


# Parameter Efficient Fine-Tuning of Segment Anything Model

Carolin Teuber<sup>\*1,2</sup> 

CAROLIN.TEUBER@STUD.UNI-GOETTINGEN.DE

Anwai Archit<sup>\*2</sup> 

ANWAI.ARCHIT@UNI-GOETTINGEN.DE

Constantin Pape<sup>2</sup> 

CONSTANTIN.PAPE@INFORMATIK.UNI-GOETTINGEN.DE

<sup>1</sup> *Georg-August-University Göttingen, Institute of Physics*

<sup>2</sup> *Georg-August-University Göttingen, Institute of Computer Science*

## Abstract

Segmentation is an important analysis task for biomedical images, enabling the study of individual organelles, cells or organs. Deep learning has massively improved segmentation methods, but challenges remain in generalization to new conditions, requiring costly data annotation. Vision foundation models, such as Segment Anything Model (SAM), address this issue through broad segmentation capabilities. However, these models still require finetuning on annotated data, although with less annotations, to achieve optimal results for new conditions. As a downside, they require more computational resources. This makes parameter-efficient finetuning (PEFT) relevant for their application. We contribute the first comprehensive study of PEFT for SAM applied to biomedical segmentation by evaluating 9 PEFT methods on diverse datasets. We also provide an implementation of QLoRA for vision transformers and a new approach for resource-efficient finetuning of SAM.

**Keywords:** segment anything, peft, biomedical image segmentation

## 1. Introduction

Segmentation is a fundamental analysis task for biomedical images. It enables the study of individual objects, such as cells and organelles in microscopy, or organs and lesions in medical imaging. Deep learning has massively advanced the field. However, the large diversity of modalities and tasks so far required different methods for specific applications, such as CellPose ([Pachitariu and Stringer, 2022](#)) and Stardist ([Schmidt et al., 2018](#)) for cell and nucleus segmentation, or nnU-Net ([Isensee et al., 2020](#)) and TotalSegmentator ([Wasserthal et al., 2023](#)) for segmentation in radiology. Adapting any of these models to a new modality or a new segmentation task requires further data annotation for training due to limited generalisation. Annotations can only be provided by experts and is time-consuming, making adaptation costly and preventing the wider use of automatic segmentation.

Vision foundation models for image segmentation, e.g. Segment Anything Model (SAM) ([Kirillov et al., 2023](#)) or SEEM ([Zou et al., 2023](#)), promise a more unified solution. These models have been trained on large annotated datasets and address both interactive and automatic segmentation. They were recently adapted to biomedical images, resulting in foundation models for microscopy ([Archit et al., 2023](#); [Israel et al., 2024](#)) and medical imaging ([Ma et al., 2024](#); [Zhao et al., 2024](#); [Archit et al., 2025](#)). These models are applicable to many tasks in their respective domain without adaptation, but specific finetuning can further improve them ([Archit et al., 2023](#)). Notably, they need fewer annotated data compared to other models, requiring as few as a single labeled image ([Zhou et al., 2024](#)).

---

\* Contributed Equally

Most vision foundation models use a vision transformer (ViT) (Dosovitskiy et al., 2021) as encoder. Hence, they typically have more parameters than previous architectures, making training more resource demanding and requiring a high-end GPU, even for small training sets. To enable efficient adaptation, parameter-efficient finetuning (PEFT) has emerged, for example through low rank adaptation of attention layers (LoRA) (Hu et al., 2021). Instead of updating all model parameters, these methods either update only a small subset of parameters, or they introduce a few new parameters that are updated, while freezing the rest of the model. While PEFT has been extensively studied for large language models (Pu et al., 2023; Xu et al., 2023; Balne et al., 2024), its application in computer vision, particularly for segmentation tasks, is less explored. Several approaches that adapt foundation models to biomedical segmentation use PEFT, e.g. (Archit et al., 2023; Zhou et al., 2024) for microscopy and (Gu et al., 2024; Zhang and Liu, 2023; Wei et al., 2024) for medical imaging. However, they primarily use LoRA without investigating hyperparameters or alternatives. Prior work has studied PEFT for classification in natural images (Xin et al., 2024) as well as classification and text-to-image generation in medical images (Dutt et al., 2024).

We address this gap by studying PEFT for biomedical segmentation; for SAM and its variants  $\mu$ SAM (Archit et al., 2023) and MedicoSAM (Archit et al., 2025). We contribute:

- An evaluation of 9 PEFT methods on 6 microscopy and 6 medical imaging datasets.
- An implementation of quantized LoRA (QLoRA) (Dettmers et al., 2023) for ViTs.
- Recommendations for the use of PEFT and a workflow for efficient adaptation of SAM to new segmentation tasks.
- A detailed ablation of hyperparameters for several PEFT methods, including LoRA.

Our workflow and improvements from efficient adaptation are shown in Fig. 1. We believe that our study will facilitate the use of foundation models for biomedical image segmentation. Further, it will inform future developments of PEFT for computer vision. Our code is available at <https://github.com/computational-cell-analytics/peft-sam>.

## 2. Methods

### 2.1. Additive and Selective Finetuning

We distinguish two types of methods: additive and selective PEFT. Selective methods update a subset of the model parameters, while freezing the rest. A simple example is freezing parts of the model, for example SAM’s image encoder, mask decoder, or prompt encoder. Freezing the image encoder, which contains most parameters, yields the greatest efficiency gain. (Archit et al., 2023) have shown that this approach does not have a large negative impact on segmentation quality after finetuning. We refer to this approach as Freeze Encoder. The other selective PEFT methods we study are LayerNorm Tuning (LN Tune) (Basu et al., 2023), Bias Tuning (Bias Tune) (Cai et al., 2021), and Attention Tuning (Attn Tune). (Touvron et al., 2022), which update only the parameters of the normalization layers, the biases, or the attention weights, respectively.

Additive PEFT methods introduce a few additional parameters, while freezing the existing ones. Among these methods, LoRA (Hu et al., 2021) reduces the number of parameters

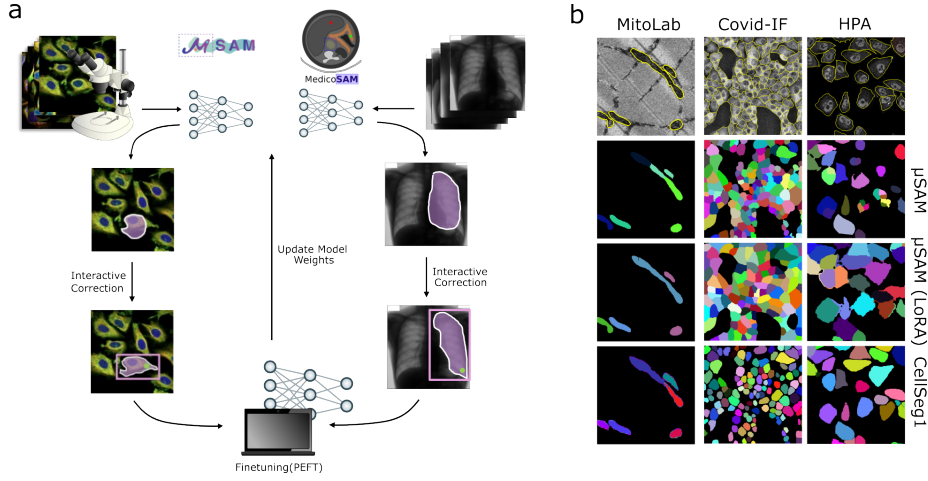


Figure 1: Overview of PEFT-SAM. a) We study PEFT of domain-specific SAMs to enable interactive correction and efficient finetuning for improved segmentation. b) Segmentation results for three datasets from  $\mu$ SAM,  $\mu$ SAM finetuned on two images with LoRA and CellSeg1 (Zhou et al., 2024).

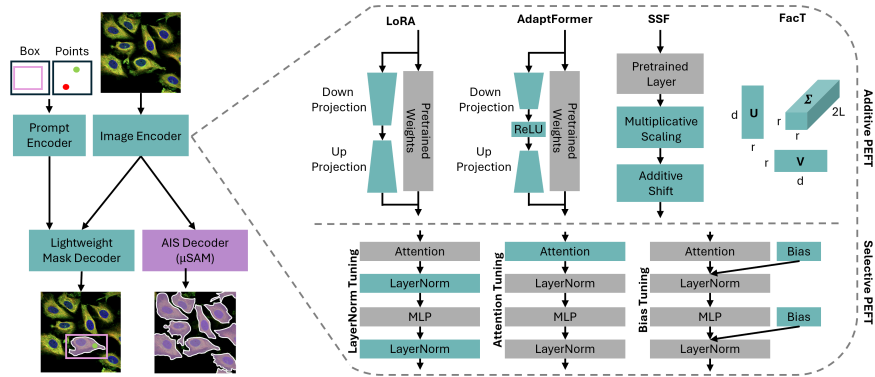


Figure 2: The original architecture of SAM, comprising image encoder, mask decoder, and prompt encoder. The image encoder is fine-tuned through additive PEFT, which introduces a few additional parameters, or selective PEFT, which updates only selected parameters. We study 9 methods; freezing the image encoder not shown.

via a low rank decomposition of the attention weight matrix:

$$\mathbf{W} = \mathbf{W}_{pretrained} + \alpha \mathbf{A} \mathbf{B}, \tag{1}$$

where  $\mathbf{A} \in \mathbb{R}^{d \times r}$ ,  $\mathbf{B} \in \mathbb{R}^{r \times d}$ . Here, the rank  $r$  is much smaller than the original dimension  $d$  of  $\mathbf{W}$ .  $\alpha$  scales the learned weights. Further efficiency gains can be obtained by quantiz-

ing the frozen weights, i.e.  $W_{pretrained}$  and others, to 4 bit during training, as in QLoRA (Detmers et al., 2023). We adopt this approach for ViTs, providing, to our knowledge, the first application in computer vision. AdaptFormer (Chen et al., 2022) adds a lightweight module, consisting of two fully connected layers, in parallel to the MLP layers of the ViT. The outputs of the adapter are scaled by a factor  $\alpha$  and added to the original MLP outputs. Scale-Shift Features (SSF) (Lian et al., 2023) performs a linear transformation, introducing a scale and a shift parameter to the output of each layer in the transformer block. Factor Tuning (FacT) (Jie and Deng, 2023) combines multiple weight matrices into a single tensor and then applies a low rank decomposition to it. Here, we adopt the implementation of (Chen et al., 2024a), which tensorizes the attention weight increment matrices (corresponding to  $A, B$  in Eq. 1) and then decomposes the tensor according to:

$$\Delta \mathbf{W} = \mathbf{U} \Sigma \mathbf{V}^T, \quad (2)$$

where  $\mathbf{U} \in \mathbb{R}^{d \times r}$ ,  $\mathbf{V} \in \mathbb{R}^{d \times r}$  and  $\Sigma \in \mathbb{R}^{r \times r}$ . The factors  $\mathbf{U}$  and  $\mathbf{V}$  are shared across layers.

Fig. 2 shows an overview of these 9 PEFT methods. We apply them only to the image encoder; prompt encoder and mask decoder are always updated. We also compare these methods with normal parameter updates (Full FT). We use SAM (Kirillov et al., 2023) and two domain-specific models,  $\mu$ SAM (Archit et al., 2023) for microscopy, and MedicoSAM (Archit et al., 2025) for medical imaging, to initialize weights. The latter two models have finetuned SAM on a large annotated dataset from the respective domain.

## 2.2. Interactive Segmentation

SAM has introduced a novel formulation for interactive segmentation, where users can provide input prompts, points (positive or negative), a bounding box or a rough mask, to identify an object. The model then predicts the corresponding mask by processing the image with its image encoder, a ViT, the prompts with its prompt encoder, and the outputs of image encoder and prompt encoder with its mask decoder. Model predictions can be corrected by providing further prompts.

SAM is trained on a large dataset with annotations using an objective that simulates interactive segmentation. In each iteration, this objective first samples prompts from an annotated mask, predicts the object mask, and then iteratively corrects the prediction with additional prompts sampled from the annotation. Predictions and annotations are compared with a loss function for each iteration, and the average loss is used to update parameters. We use the implementation of this procedure from (Archit et al., 2023).

To evaluate interactive segmentation, we automatically derive prompts from annotated masks to segment the object and then iteratively correct the segmentation, similar to the training objective. We perform 7 correction iterations. We compute the segmentation metric (App. A) between annotations and predictions for the initial prompt and corrections. We report the results for an initial point prompt, an initial box prompt, and the last correction iteration, when starting from a point ( $I_P$ ), and when starting from a box ( $I_B$ ).

## 2.3. Automatic Instance Segmentation

For automatic instance segmentation (AIS) we use the implementation of  $\mu$ SAM, which adds a UNETR decoder (Hatamizadeh et al., 2021) to SAM to predict outputs for instance



segmentation. The decoder consists of four blocks, with two convolutional layers and a transposed convolution for upsampling each. The blocks also receive the image encoder’s output as input. The decoder predicts three channels: the distance to the object center, the distance to the object boundary, and foreground probabilities. During training, it is updated jointly with the rest of SAM, using the annotations to derive targets for its outputs.

During inference, the segmentation is computed by deriving seeds from the distance predictions, a mask from foreground predictions, and applying a seeded watershed inside this mask. For evaluation, the instance segmentation is compared with annotations using the mean segmentation accuracy, see App. A.

## 2.4. Data

We use 6 microscopy and 6 medical imaging datasets. For light microscopy (LM), we use Covid-IF (Pape et al., 2021) with 49 immunofluorescence microscopy images and cell annotations, HPA (Ouyang et al., 2019) with 276 confocal microscopy images and cell annotations; using the channel that stains cytosol. We use GoNuclear (Vijayan et al., 2024) with 5 fluorescence microscopy and nucleus annotations. We use OrgaSegment (Lefferts et al., 2024) with 231 brightfield microscopy images and organoid annotations. We use two electron microscopy (EM) datasets: Platynereis (Vergara et al., 2021) with 3 EM volumes and cilia annotations, and a subset of MitoLab (Conrad and Narayan, 2023) with a volume of glycolytic muscles and mitochondria annotations. For the 3D datasets (GoNuclear, Platynereis, MitoLab), we perform 2D segmentation by treating slices as individual images.

For medical imaging, we use AMD-SD (Hu et al., 2024) with 3049 optical coherence tomograms and annotations for lesions. We use JSRT (Shiraishi et al., 2000) with 247 images and lung and heart annotations. We use Mice TumSeg (Jensen et al., 2024) with 452 micro-CT volumes and tumor annotations. We use Papila (Kovalyk et al., 2022) with 488 fundus images and optic cup annotations. We use MOTUM (Gong et al., 2024) with 64 brain MRI volumes and tumor annotations. We use PSFHS (Chen et al., 2024b) with 1358 ultrasound images and fetal head and pubic symphysis annotations. For the 3D datasets (MOTUM and Mice TumSeg), we perform 2D segmentation (see above).

## 3. Results

### 3.1. Comparison of PEFT methods

We evaluate the PEFT methods (Sec. 2.1), on 6 microscopy datasets (Sec. 2.4) for interactive and automatic segmentation. We use SAM and  $\mu$ SAM (either LM or EM model) as base models. Models are trained with a batch size of 2 and 25 objects per image, using a A100 GPU with 80GB of VRAM. We use separate train / test splits for all datasets.

The results are shown in Fig. 3. Finetuning improves over the base models, depending on the task and the base model. Iterative segmentation ( $I_B$ ,  $I_P$ ) shows the smallest improvements, other tasks improve more. The effectiveness of PEFT methods differs across datasets. Full finetuning typically improves most, LoRA is the best overall PEFT method. QLoRA shows worse performance with SAM as base model, but not for  $\mu$ SAM. The results are summarized in Tab. 1 (SAM) and Tab. 2 ( $\mu$ SAM). We perform ablation studies for LoRA, Adaptformer and FacT in App. D. We also perform experiments for the 6 medical

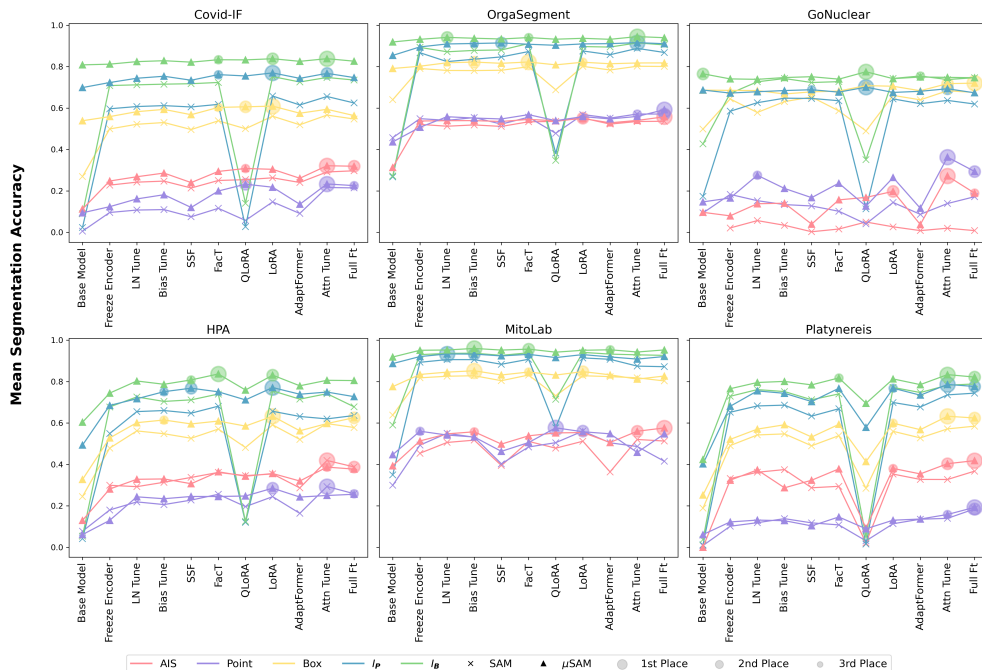


Figure 3: PEFT results for automatic and interactive microscopy segmentation. Methods are ordered by parameter count, SAM and  $\mu$ SAM are used as base models. Circles show the best three results per dataset and task. See Fig. 7 for examples.

datasets. Here, we use SAM and MedicoSAM as base models and do not evaluate AIS, otherwise using the same settings. The results are shown in Fig. 4 and summarized in Tabs 3,4. We see the same trends as for microscopy.

We also evaluate the computational efficiency of PEFT methods. Tabs. 5, 6, 7 report the parameter count, memory efficiency, and training times for ViT-B, ViT-L and ViT-H. Fig. 8 shows the training times for microscopy. Overall, PEFT methods only yield marginal efficiency gains for ViT-B and ViT-L, with the exception of Freeze Encoder, and small gains for ViT-H. As a preliminary conclusion, PEFT methods generally don't lead to better segmentation quality than full finetuning. Their efficiency gains are minor, except for Freeze Encoder. LoRA and, for small domain gaps, QLoRA provide relatively good quality-efficiency trade-offs.

### 3.2. Resource-efficient Finetuning

Building on the evaluation of PEFT methods, we propose resource-efficient finetuning by adopting a similar workflow to CellSeg1 (Zhou et al., 2024), who finetune SAM for automatic segmentation on a single image using LoRA. We compare their method with our finetuning approach for automatic *and* interactive segmentation, using Freeze Encoder, QLoRA, LoRA, and Full Finetuning, which offer the best efficiency-quality trade-offs. For more efficiency,

## PEFT-SAM

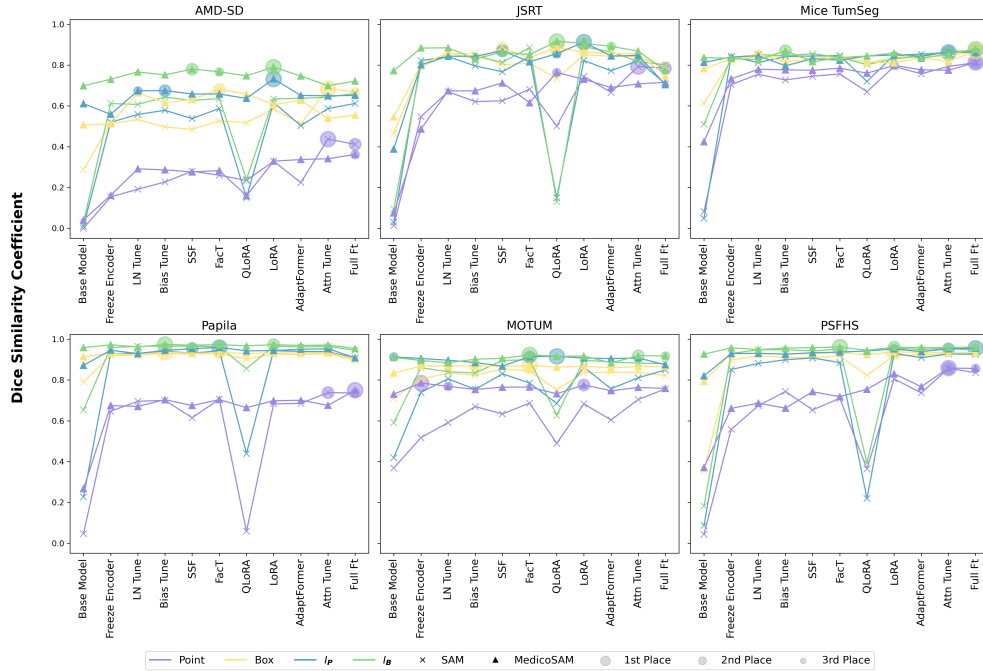


Figure 4: PEFT results for medical imaging. MedicoSAM is used as domain-specific base model and we do not evaluate AIS, otherwise same settings as for microscopy.

we lower the number of objects per image to 5, otherwise using the same settings as in Sec. 3.1. We use one image for training, one for validation, and the same test sets as before. Fig. 5 shows the results. SAM improves for all tasks,  $\mu$ SAM mainly for AIS. Our approach is on par with CellSeg1, for which we also use both base models, while improving interactive segmentation. Interestingly, full finetuning is on par with PEFT, despite the small training data and more trainable parameters. For large domain shifts (Platynereis) it outperforms PEFT. We also benchmark efficiency, see Tabs. 8, 9, 10. Here, we again see major gains when freezing the encoder, and small gains from other PEFT.

## 4. Discussion

We conduct a thorough study of PEFT for segmentation in biomedical images with SAM. Our experiments show that PEFT achieves a similar quality as full finetuning. Contrary to observations made by others, e.g. (Dutt et al., 2024), it does not lead to better results for limited training data. The performance of PEFT methods varies across datasets, LoRA is the best overall, QLoRA is good for small domain gaps. Efficiency gains are marginal for small models (ViT-B, ViT-L) and small for larger models (ViT-H). An exception is encoder freezing, which leads to clear gains, without a strong negative impact on quality. Given these results, we recommend freezing the encoder in limited resource settings, exploring

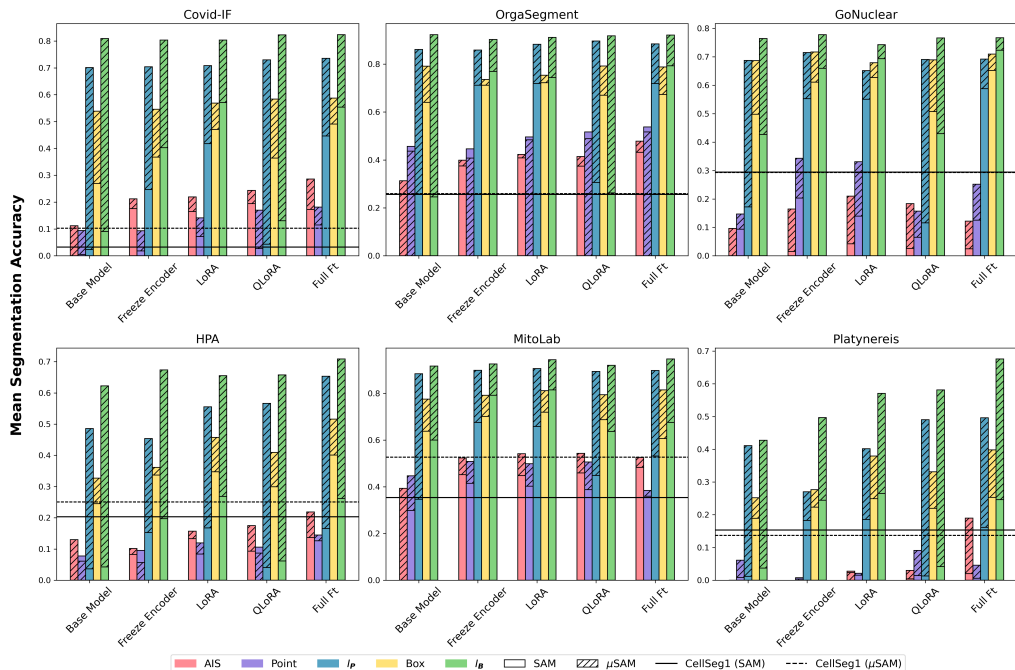


Figure 5: Resource-efficient training for microscopy segmentation. Our methods use one image for training, one for validation, CellSeg1 uses only a single image.

QLoRA or LoRA with medium resources, which may enable training despite only small efficiency benefits, and otherwise using full finetuning.

We propose an approach for resource-efficient finetuning, which can improve SAM with only two annotated image, similar to (Zhou et al., 2024), but also improving interactive segmentation. We believe that this approach will speed up many practical segmentation tasks, by enabling finetuning SAM previously hindered by resource demands. To this end, we will implement our approach in the  $\mu$ SAM tool, which provides interactive data annotation, enabling efficient human-in-the-loop annotation and training in one tool.

Finally, we believe that our work will benefit future work on PEFT for vision foundation models, e.g. for SAM2 (Ravi et al., 2024). We also show a need to improve PEFT for segmentation; current methods do not yield clear advantages in the quality-efficiency trade-off. Such improvements may be achieved by simple strategies, such as using adapters in a subset of layers, or through more fundamental advances.

## Acknowledgments

The work of Anwai Archit was funded by the Deutsche Forschungsgemeinschaft (DFG, German Research Foundation) - PA 4341/2-1. This work was also supported by the Google Research Scholarship “Vision Foundation Models for Bioimage Segmentation”. We gratefully acknowledge the computing time granted by the Resource Allocation Board and provided on the supercomputer Emmy at NHR@Göttingen as part of the NHR infrastructure, under the project nim00007. We acknowledge the use of icons from Bioicons ([Jug and Contributors, 2023](#)) in Fig. 1. In particular, the microscope icon by DBCLS ([for Life Science , DBCLS](#)) is licensed under CC-BY 4.0.

## References

- Anwai Archit, Sushmita Nair, Nabeel Khalid, Paul Hilt, Vikas Rajashekar, Marei Freitag, Sagnik Gupta, Andreas Dengel, Sheraz Ahmed, and Constantin Pape. Segment anything for microscopy, 2023. URL <https://www.biorxiv.org/content/early/2023/08/22/2023.08.21.554208>.
- Anwai Archit, Luca Freckmann, and Constantin Pape. Medicosam: Towards foundation models for medical image segmentation, 2025. URL <https://arxiv.org/abs/2501.11734>.
- Charith Chandra Sai Balne, Sreyoshi Bhaduri, Tamoghna Roy, Vinija Jain, and Aman Chadha. Parameter efficient fine tuning: A comprehensive analysis across applications, 2024. URL <https://arxiv.org/abs/2404.13506>.
- Samyadeep Basu, Daniela Massiceti, Shell Xu Hu, and Soheil Feizi. Strong baselines for parameter efficient few-shot fine-tuning, 2023. URL <https://arxiv.org/abs/2304.01917>.
- Han Cai, Chuang Gan, Ligeng Zhu, and Song Han. Tinytl: Reduce activations, not trainable parameters for efficient on-device learning, 2021. URL <https://arxiv.org/abs/2007.11622>.
- Juan C. Caicedo, Allen Goodman, Kyle W. Karhohs, Beth A. Cimini, Jeanelle Ackerman, Marzieh Haghighi, CherKeng Heng, Tim Becker, Minh Doan, Claire McQuin, Mohammad Rohban, Shantanu Singh, and Anne E. Carpenter. Nucleus segmentation across imaging experiments: the 2018 data science bowl. *Nature Methods*, 16(12):1247–1253, 2019. ISSN 1548-7105. doi: 10.1038/s41592-019-0612-7. URL <https://doi.org/10.1038/s41592-019-0612-7>.
- Cheng Chen, Juzheng Miao, Dufan Wu, Aoxiao Zhong, Zhiling Yan, Sekeun Kim, Jiang Hu, Zhengliang Liu, Lichao Sun, Xiang Li, et al. Ma-sam: Modality-agnostic sam adaptation for 3d medical image segmentation. *Medical Image Analysis*, 98:103310, 2024a. URL <https://doi.org/10.1016/j.media.2024.103310>.
- Gaowen Chen, Jieyun Bai, Zhanhong Ou, Yaosheng Lu, and Huijin Wang. Psfhs: Intrapartum ultrasound image dataset for ai-based segmentation of pubic symphysis and fetal head. *Scientific Data*, 11(1), May 2024b. ISSN 2052-4463. doi: 10.1038/s41597-024-03266-4. URL <http://doi.org/10.1038/s41597-024-03266-4>.

- Shoufa Chen, Chongjian Ge, Zhan Tong, Jiangliu Wang, Yibing Song, Jue Wang, and Ping Luo. Adaptformer: Adapting vision transformers for scalable visual recognition, 2022. URL <https://arxiv.org/abs/2205.13535>.
- Ryan Conrad and Kedar Narayan. Instance segmentation of mitochondria in electron microscopy images with a generalist deep learning model trained on a diverse dataset. *Cell Systems*, 14(1):58–71.e5, 2023. ISSN 2405-4712. doi: 10.1016/j.cels.2022.12.006. URL <https://doi.org/10.1016/j.cels.2022.12.006>.
- Tim Dettmers, Artidoro Pagnoni, Ari Holtzman, and Luke Zettlemoyer. Qlora: Efficient finetuning of quantized llms, 2023. URL <https://arxiv.org/abs/2305.14314>.
- Alexey Dosovitskiy, Lucas Beyer, Alexander Kolesnikov, Dirk Weissenborn, Xiaohua Zhai, Thomas Unterthiner, Mostafa Dehghani, Matthias Minderer, Georg Heigold, Sylvain Gelly, Jakob Uszkoreit, and Neil Houlsby. An image is worth 16x16 words: Transformers for image recognition at scale, 2021. URL <https://arxiv.org/abs/2010.11929>.
- Raman Dutt, Linus Ericsson, Pedro Sanchez, Sotirios A. Tsaftaris, and Timothy Hospedales. Parameter-efficient fine-tuning for medical image analysis: The missed opportunity. In *Medical Imaging with Deep Learning*, 2024. URL <https://openreview.net/forum?id=LVRhXa0q5r>.
- Christoffer Edlund, Timothy R. Jackson, Nabeel Khalid, Nicola Bevan, Timothy Dale, Andreas Dengel, Sheraz Ahmed, Johan Trygg, and Rickard Sjögren. Livecell—a large-scale dataset for label-free live cell segmentation. *Nature Methods*, 18(9):1038–1045, 2021. doi: 10.1038/s41592-021-01249-6. URL <https://doi.org/10.1038/s41592-021-01249-6>.
- Database Center for Life Science (DBCLS). Togotv - life science video portal, 2023. URL <https://togotv.dbcls.jp/en/pics.html>.
- Zhenyu Gong, Tao Xu, Nan Peng, Xing Cheng, Chen Niu, Benedikt Wiestler, Fan Hong, and Hongwei Bran Li. A multi-center, multi-parametric mri dataset of primary and secondary brain tumors. *Scientific Data*, 11(1), July 2024. ISSN 2052-4463. doi: 10.1038/s41597-024-03634-0. URL <http://doi.org/10.1038/s41597-024-03634-0>.
- Hanxue Gu, Haoyu Dong, Jichen Yang, and Maciej A. Mazurowski. How to build the best medical image segmentation algorithm using foundation models: a comprehensive empirical study with segment anything model, 2024. URL <https://arxiv.org/abs/2404.09957>.
- Ali Hatamizadeh, Yucheng Tang, Vishwesh Nath, Dong Yang, Andriy Myronenko, Bennett Landman, Holger Roth, and Daguang Xu. Unetr: Transformers for 3d medical image segmentation, 2021. URL <https://arxiv.org/abs/2103.10504>.
- Edward J. Hu, Yelong Shen, Phillip Wallis, Zeyuan Allen-Zhu, Yuanzhi Li, Shean Wang, Lu Wang, and Weizhu Chen. Lora: Low-rank adaptation of large language models, 2021. URL <https://arxiv.org/abs/2106.09685>.



- Yunwei Hu, Yundi Gao, Weihao Gao, Wenbin Luo, Zhongyi Yang, Fen Xiong, Zidan Chen, Yucai Lin, Xinjing Xia, Xiaolong Yin, Yan Deng, Lan Ma, and Guodong Li. Amd-sd: An optical coherence tomography image dataset for wet amd lesions segmentation. *Scientific Data*, 11(1), September 2024. ISSN 2052-4463. doi: 10.1038/s41597-024-03844-6. URL <http://doi.org/10.1038/s41597-024-03844-6>.
- Fabian Isensee, Paul F. Jaeger, Simon A. A. Kohl, Jens Petersen, and Klaus H. Maier-Hein. nnu-net: a self-configuring method for deep learning-based biomedical image segmentation. *Nature Methods*, 18(2):203–211, December 2020. ISSN 1548-7105. doi: 10.1038/s41592-020-01008-z. URL <http://doi.org/10.1038/s41592-020-01008-z>.
- Uriah Israel, Markus Marks, Rohit Dilip, Qilin Li, Changhua Yu, Emily Laubscher, Shenyi Li, Morgan Schwartz, Elora Pradhan, Ada Ates, et al. A foundation model for cell segmentation. *bioRxiv*, pages 2023–11, 2024. URL <https://www.biorxiv.org/content/10.1101/2023.11.17.567630v3>.
- Malte Jensen, Andreas Clemmensen, Jacob Gorm Hansen, Julie van Krimpen Mortensen, Emil N. Christensen, Andreas Kjaer, and Rasmus Sejersten Ripa. 3d whole body pre-clinical micro-ct database of subcutaneous tumors in mice with annotations from 3 annotators. *Scientific Data*, 11(1), September 2024. ISSN 2052-4463. doi: 10.1038/s41597-024-03814-y. URL <http://doi.org/10.1038/s41597-024-03814-y>.
- Shibo Jie and Zhi-Hong Deng. Fact: Factor-tuning for lightweight adaptation on vision transformer, 2023. URL <https://arxiv.org/abs/2212.03145>.
- Florian Jug and Bioicons Contributors. Bioicons - free biology icons, 2023. URL <https://bioicons.com/>.
- Alexander Kirillov, Eric Mintun, Nikhila Ravi, Hanzi Mao, Chloe Rolland, Laura Gustafson, Tete Xiao, Spencer Whitehead, Alexander C. Berg, Wan-Yen Lo, Piotr Dollár, and Ross Girshick. Segment anything, 2023. URL <https://arxiv.org/abs/2304.02643>.
- Oleksandr Kovalyk, Juan Morales-Sánchez, Rafael Verdú-Monedero, Inmaculada Sellés-Navarro, Ana Palazón-Cabanes, and José-Luis Sancho-Gómez. Papila: Dataset with fundus images and clinical data of both eyes of the same patient for glaucoma assessment. *Scientific Data*, 9(1), June 2022. ISSN 2052-4463. doi: 10.1038/s41597-022-01388-1. URL <http://doi.org/10.1038/s41597-022-01388-1>.
- Juliet W. Lefferts, Suzanne Kroes, Matthew B. Smith, Paul J. Niemöller, Natascha D. A. Nieuwenhuijze, Heleen N. Sonneveld van Kooten, Cornelis K. van der Ent, Jeffrey M. Beekman, and Sam F. B. van Beuningen. Orgasegment: deep-learning based organoid segmentation to quantify cftr dependent fluid secretion. *Communications Biology*, 7(1): 319, 2024. ISSN 2399-3642. doi: 10.1038/s42003-024-05966-4. URL <https://doi.org/10.1038/s42003-024-05966-4>.
- Dongze Lian, Daquan Zhou, Jiashi Feng, and Xinchao Wang. Scaling & shifting your features: A new baseline for efficient model tuning, 2023. URL <https://arxiv.org/abs/2210.08823>.

- Jun Ma, Yuting He, Feifei Li, Lin Han, Chenyu You, and Bo Wang. Segment anything in medical images. *Nature Communications*, 15(1):654, 2024. URL <https://www.nature.com/articles/s41467-024-44824-z>.
- Wei Ouyang, Casper F. Winsnes, Martin Hjelmare, Anthony J. Cesnik, Lovisa Åkesson, Hao Xu, Devin P. Sullivan, Shubin Dai, Jun Lan, Jinmo Park, Shaikat M. Galib, Christof Henkel, Kevin Hwang, Dmytro Poplavskiy, Bojan Tunguz, Russel D. Wolfinger, Yinzheng Gu, Chuanpeng Li, Jinbin Xie, Dmitry Buslov, Sergei Fironov, Alexander Kiselev, Dmytro Panchenko, Xuan Cao, Runmin Wei, Yuanhao Wu, Xun Zhu, Kuan-Lun Tseng, Zhifeng Gao, Cheng Ju, Xiaohan Yi, Hongdong Zheng, Constantin Kappel, and Emma Lundberg. Analysis of the human protein atlas image classification competition. *Nature Methods*, 16(12):1254–1261, 2019. ISSN 1548-7105. doi: 10.1038/s41592-019-0658-6. URL <https://doi.org/10.1038/s41592-019-0658-6>.
- Marius Pachitariu and Carsen Stringer. Cellpose 2.0: how to train your own model. *Nature Methods*, 19(12):1634–1641, December 2022. ISSN 1548-7105. doi: 10.1038/s41592-022-01663-4. URL <https://doi.org/10.1038/s41592-022-01663-4>.
- Constantin Pape, Roman Remme, Adrian Wolny, Sylvia Olberg, Steffen Wolf, Lorenzo Cerrone, Mirko Cortese, Severina Klaus, Bojana Lucic, Stephanie Ullrich, Maria Anders-Össwein, Stefanie Wolf, Berati Cerikan, Christopher J. Neufeldt, Markus Ganter, Paul Schnitzler, Uta Merle, Marina Lusic, Steeve Boulant, Megan Stanifer, Ralf Barten-schlager, Fred A. Hamprecht, Anna Kreshuk, Christian Tischer, Hans-Georg Kräusslich, Barbara Müller, and Vibor Laketa. Microscopy-based assay for semi-quantitative detection of sars-cov-2 specific antibodies in human sera. *BioEssays*, 43(3):2000257, 2021. doi: <https://doi.org/10.1002/bies.202000257>. URL <https://onlinelibrary.wiley.com/doi/abs/10.1002/bies.202000257>.
- George Pu, Anirudh Jain, Jihan Yin, and Russell Kaplan. Empirical analysis of the strengths and weaknesses of peft techniques for llms, 2023. URL <https://arxiv.org/abs/2304.14999>.
- Nikhila Ravi, Valentin Gabeur, Yuan-Ting Hu, Ronghang Hu, Chaitanya Ryali, Tengyu Ma, Haitham Khedr, Roman Rädle, Chloe Rolland, Laura Gustafson, et al. Sam 2: Segment anything in images and videos. *arXiv preprint arXiv:2408.00714*, 2024. URL <https://arxiv.org/abs/2408.00714>.
- Uwe Schmidt, Martin Weigert, Coleman Broaddus, and Gene Myers. *Cell Detection with Star-Convex Polygons*, page 265–273. Springer International Publishing, 2018. ISBN 9783030009342. doi: 10.1007/978-3-030-00934-2\_30. URL [http://doi.org/10.1007/978-3-030-00934-2\\_30](http://doi.org/10.1007/978-3-030-00934-2_30).
- Junji Shiraishi, Shigehiko Katsuragawa, Junpei Ikezoe, Tsuneo Matsumoto, Takeshi Kobayashi, Ken-ichi Komatsu, Mitate Matsui, Hiroshi Fujita, Yoshie Kodera, and Kunio Doi. Development of a digital image database for chest radiographs with and without a lung nodule: Receiver operating characteristic analysis of radiologists’ detection of pulmonary nodules. *American Journal of Roentgenology*, 174(1):71–74, January 2000. ISSN

- 1546-3141. doi: 10.2214/ajr.174.1.1740071. URL <http://doi.org/10.2214/ajr.174.1.1740071>.
- Hugo Touvron, Matthieu Cord, Alaaeldin El-Nouby, Jakob Verbeek, and Hervé Jégou. Three things everyone should know about vision transformers, 2022. URL <https://arxiv.org/abs/2203.09795>.
- Hernando M. Vergara, Constantin Pape, Kimberly I. Meechan, Valentyna Zinchenko, Christel Genoud, Adrian A. Wanner, Kevin Nzumbi Mutemi, Benjamin Titze, Rachel M. Templin, Paola Y. Bertucci, Oleg Simakov, Wiebke Dürichen, Pedro Machado, Emily L. Savage, Lothar Schermelleh, Yannick Schwab, Rainer W. Friedrich, Anna Kreshuk, Christian Tischer, and Detlev Arendt. Whole-body integration of gene expression and single-cell morphology. *Cell*, 184(18):4819–4837.e22, 2021. ISSN 0092-8674. doi: 10.1016/j.cell.2021.07.017. URL <https://doi.org/10.1016/j.cell.2021.07.017>.
- Athul Vijayan, Tejasvinee Atul Mody, Qin Yu, Adrian Wolny, Lorenzo Cerrone, Soeren Strauss, Miltos Tsiantis, Richard S. Smith, Fred A. Hamprecht, Anna Kreshuk, and Kay Schneitz. A deep learning-based toolkit for 3d nuclei segmentation and quantitative analysis in cellular and tissue context. *Development*, 151(14):dev202800, 07 2024. ISSN 0950-1991. doi: 10.1242/dev.202800. URL <https://doi.org/10.1242/dev.202800>.
- Jakob Wasserthal, Hanns-Christian Breit, Manfred T Meyer, Maurice Pradella, Daniel Hinck, Alexander W Sauter, Tobias Heye, Daniel T Boll, Joshy Cyriac, Shan Yang, et al. Totalsegmentator: robust segmentation of 104 anatomic structures in ct images. *Radiology: Artificial Intelligence*, 5(5), 2023. URL <https://doi.org/10.1148/ryai.230024>.
- Xiaobao Wei, Jiajun Cao, Yizhu Jin, Ming Lu, Guangyu Wang, and Shanghang Zhang. I-medsam: Implicit medical image segmentation with segment anything, 2024. URL <https://arxiv.org/abs/2311.17081>.
- Yi Xin, Siqi Luo, Haodi Zhou, Junlong Du, Xiaohong Liu, Yue Fan, Qing Li, and Yuntao Du. Parameter-efficient fine-tuning for pre-trained vision models: A survey, 2024. URL <https://arxiv.org/abs/2402.02242>.
- Lingling Xu, Haoran Xie, Si-Zhao Joe Qin, Xiaohui Tao, and Fu Lee Wang. Parameter-efficient fine-tuning methods for pretrained language models: A critical review and assessment, 2023. URL <https://arxiv.org/abs/2312.12148>.
- Kaidong Zhang and Dong Liu. Customized segment anything model for medical image segmentation, 2023. URL <https://arxiv.org/abs/2304.13785>.
- Theodore Zhao, Yu Gu, Jianwei Yang, Naoto Usuyama, Ho Hin Lee, Sid Kiblawi, Tristan Naumann, Jianfeng Gao, Angela Crabtree, Jacob Abel, et al. A foundation model for joint segmentation, detection and recognition of biomedical objects across nine modalities. *Nature methods*, pages 1–11, 2024. URL <https://www.nature.com/articles/s41592-024-02499-w>.
- Peilin Zhou, Bo Du, and Yongchao Xu. Cellseg1: Robust cell segmentation with one training image, 2024. URL <https://arxiv.org/abs/2412.01410>.

Xueyan Zou, Jianwei Yang, Hao Zhang, Feng Li, Linjie Li, Jianfeng Wang, Lijuan Wang, Jianfeng Gao, and Yong Jae Lee. Segment everything everywhere all at once, 2023. URL <https://arxiv.org/abs/2304.06718>.

## Appendix A. Evaluation Metric

We use the mean segmentation accuracy, following the definition of (Caicedo et al., 2019), to evaluate instance segmentation results for the microscopy datasets. It is computed based on true positives ( $TP$ ), false negatives ( $FN$ ), and false positives ( $FP$ ), derived from the intersection over union (IoU) of predicted and true objects. Specifically, a  $TP(t)$  is defined as the number of matches between predicted and true objects with an IoU above threshold  $t$ ,  $FP(t)$  correspond to the number of predicted objects minus  $TP(t)$ , and  $FN(t)$  to the number of true objects minus  $TP(t)$ . The mean segmentation accuracy is computed over multiple thresholds:

$$\text{Mean Segmentation Accuracy} = \frac{1}{|\# \text{ thresholds}|} \sum_t \frac{TP(t)}{TP(t) + FP(t) + FN(t)}.$$

Here, we use thresholds  $t \in [0.5, 0.55, 0.6, 0.65, 0.7, 0.75, 0.8, 0.85, 0.9, 0.95]$ . For each dataset, we report the average mean segmentation accuracy over images in the test set.

We use the dice coefficient to evaluate segmentation results for medical imaging because the segmentation tasks we evaluate typically only contain a single object, or objects belonging to different classes, per image. It is defined as

$$\text{Dice Coefficient} = \frac{2 * \sum p_i t_i}{\sum p_i + \sum t_i},$$

for per-pixel prediction values  $p_i$  and per pixel target values  $t_i$ . For each dataset, we report the average dice coefficient over images in the test set.

## Appendix B. PEFT Evaluation

### B.1. Segmentation Quality

Fig. 3 and Fig. 4 present a comparison of various PEFT methods across microscopy and medical datasets respectively. The PEFT methods are arranged from left to right in the order of the number of trainable parameters, with full finetuning having the most parameters. Table 5 lists the number of parameters for each method. We evaluate the methods using training from the default SAM (Kirillov et al., 2023) and from the generalist  $\mu$ -SAM models (Archit et al., 2023), where we use either the electron microscopy or light microscopy model, and from MedicoSAM (Archit et al., 2025) for medical imaging. The models are evaluated on automatic instance segmentation (AIS) for microscopy experiments, and initial prompts (point and box prompts), and iterative prompting, beginning either from a box prompt ( $I_B$ ) or a point prompt ( $I_P$ ) for both microscopy and medical imaging experiments.

As an overall trend, we observe that as the number of trainable parameters increases, the segmentation quality also tends to increase across the different datasets, demonstrating a

tradeoff between model complexity, capacity, and performance. The relative performance of the PEFT methods varies between datasets, indicating that the suitability of different PEFT methods may depend on the dataset’s characteristics, such as complexity, size, and the model’s initial performance. Despite this variation, full finetuning, Attention Tuning, and LoRA consistently show good performance; QLoRA shows good performance for the domain specific foundation models ( $\mu$ SAM, MedicoSAM), but performs bad for default SAM, which has a larger domain gap. Among the listed PEFT methods, Attention Tuning has the highest number of trainable parameters, requiring 32.5M parameters. In contrast, LoRA significantly reduces the parameter space to just 5.4M parameters, amounting to only 5.6% of the parameters used in Full Finetuning (FFT). Despite this substantial reduction, LoRA achieves performance that is on par with Attention Tuning and Full Finetuning in most cases. To simplify these observations, we averaged the performance of the different PEFT methods over all datasets in Tabs. 1 (microscopy, SAM), 2 (microscopy,  $\mu$ SAM), 3 (medical imaging, SAM), and 4 (medical imaging, MedicoSAM). LoRA consistently ranks among the top three methods, frequently alongside full fine-tuning and attention tuning, despite these methods having significantly more parameters. It is notable that for the iterative prompting task, FacT performs very well alongside LoRA. This is especially interesting because FacT is essentially an extension of LoRA, applying the low-rank decomposition to a tensorized vision transformer. Moreover, while some PEFT methods excel for specific tasks - such as Bias Tuning for Mitolab - LoRA consistently ranks among the top methods across diverse scenarios, including AIS and single point and box prompt. This makes LoRA the best PEFT choice from a segmentation quality perspective.

The strong performance of both LoRA and Attention Tuning suggests that tuning the attention weight matrices is particularly important for domain adaptation. This highlights the potential benefit of focusing on attention-based techniques when fine-tuning models for specialized tasks.

Table 1: The mean segmentation accuracy of different PEFT methods, trained from default SAM, for microscopy segmentation and averaged over all 6 datasets. (\*): 1st Place; (\*\*): 2nd Place; (\*\*\*) : 3rd Place.

PEFT Method	AIS	Point	Box	$I_p$	$I_b$
Full FT	**0.352	**0.303	***0.665	0.727	0.796
Attn Tune	*0.352	*0.308	*0.673	**0.735	**0.809
AdaptFormer	0.291	0.255	0.636	0.718	0.795
LoRA	***0.343	***0.296	**0.667	*0.741	*0.810
QLoRA	0.281	0.218	0.529	0.206	0.288
FacT	0.328	0.270	0.644	***0.730	***0.797
SSF	0.291	0.245	0.625	0.710	0.779
Bias Tune	0.334	0.279	0.644	0.724	0.788
LN Tune	0.329	0.281	0.635	0.717	0.789
Freeze Encoder	0.309	0.267	0.620	0.690	0.768

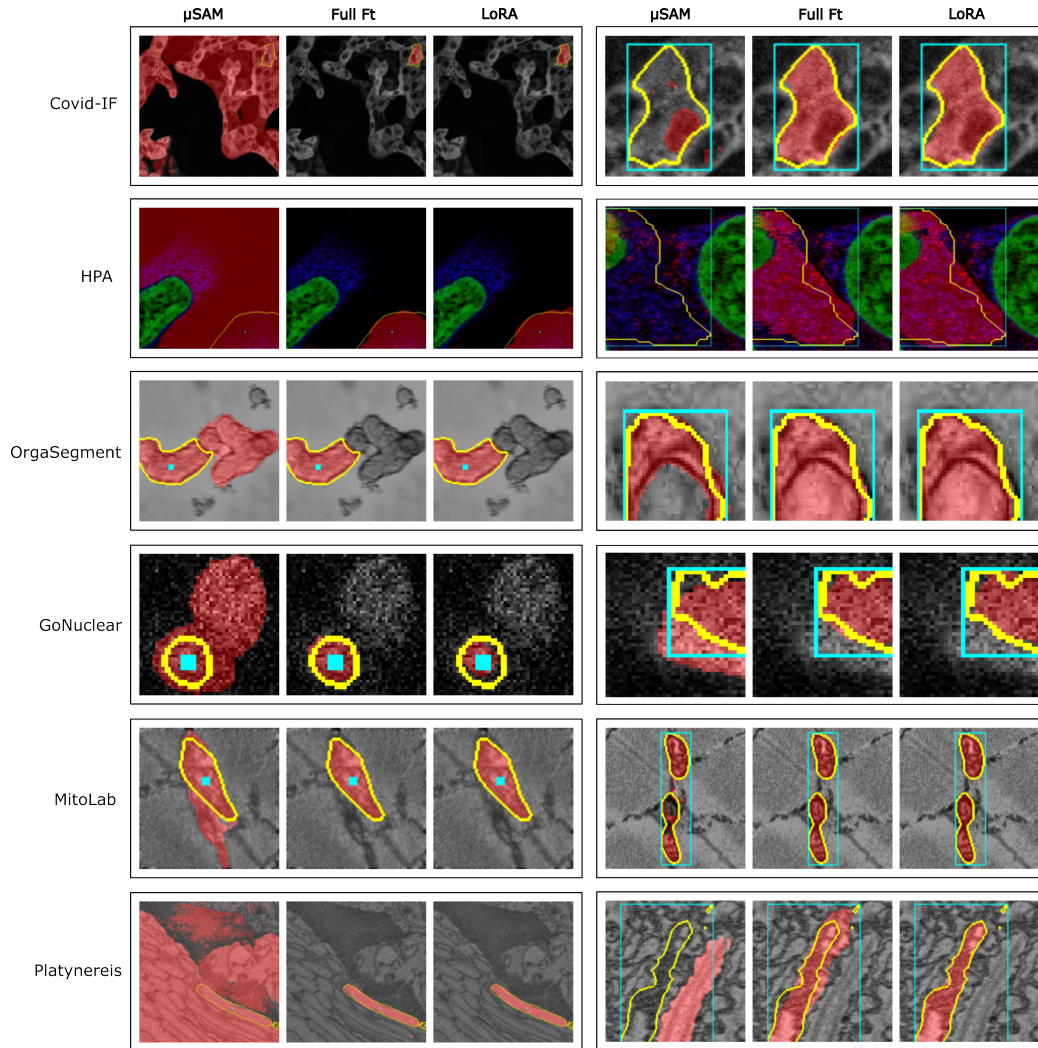


Figure 6: Qualitative comparison of interactive segmentation for the default  $\mu$ SAM model and the finetuned model with LoRA and Full Finetuning. For all three models ViT-B was used. The yellow outlines show the ground truth, red the model prediction and cyan shows the input prompts.



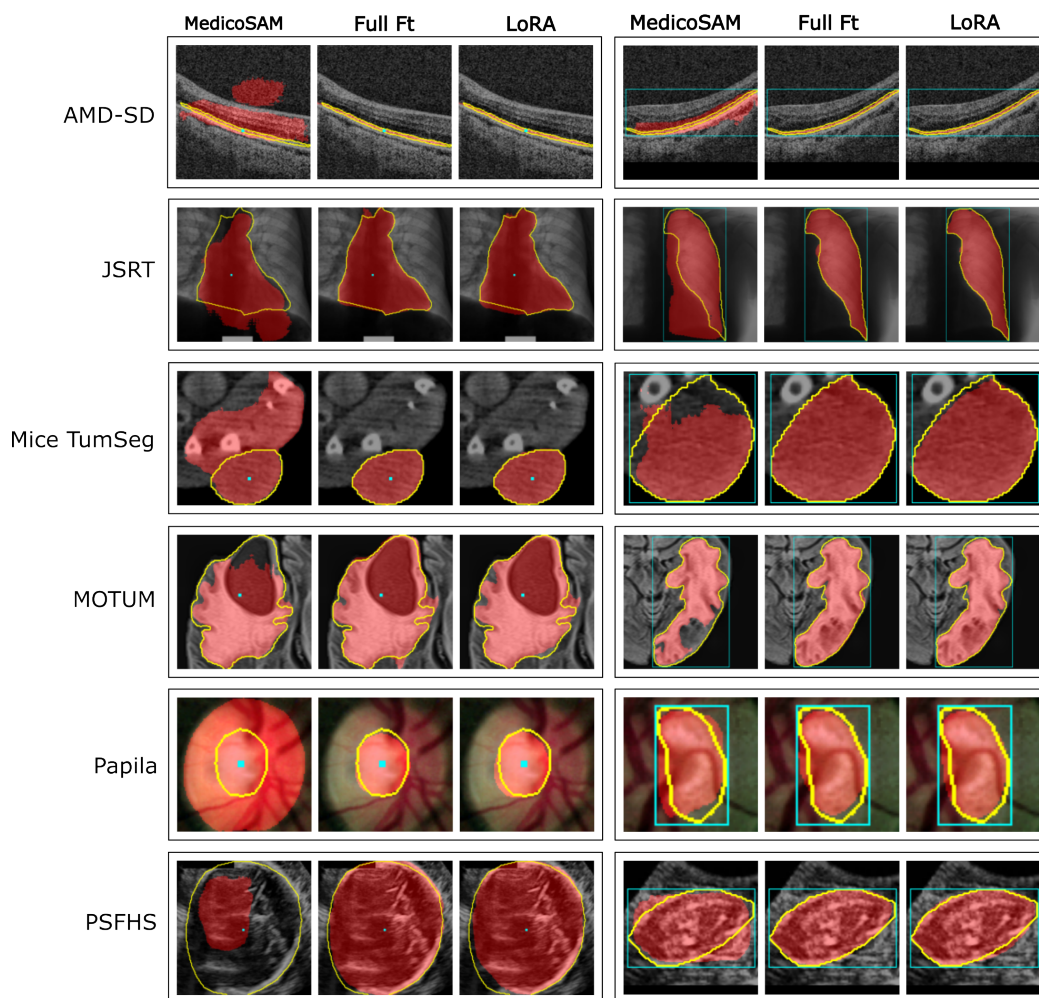


Figure 7: Qualitative comparison of interactive segmentation for the default MedicoSAM and the finetuned model with LoRA and Full Finetuning. For all three models ViT-B was used. The yellow outlines show the ground truth, red the model prediction and cyan shows the input prompts.

Table 2: The mean segmentation accuracy of different PEFT methods, trained from  $\mu$ SAM, for microscopy segmentation and averaged over all 6 datasets. (\*): 1st Place; (\*\*): 2nd Place; (\*\*\*): 3rd Place.

<b>PEFT Method</b>	<b>AIS</b>	<b>Point</b>	<b>Box</b>	<b>I<sub>p</sub></b>	<b>I<sub>b</sub></b>
Full FT	**0.406	*0.351	**0.696	0.793	0.849
Attn Tune	*0.414	**0.337	***0.695	**0.803	**0.852
AdaptFormer	0.334	0.287	0.672	0.788	0.837
LoRA	**0.390	***0.336	*0.702	*0.804	***0.852
QLoRA	0.334	0.302	0.657	0.761	0.823
FacT	0.379	0.317	0.693	***0.799	*0.854
SSF	0.324	0.274	0.670	0.789	0.842
Bias Tune	0.357	0.307	0.690	0.796	0.843
LN Tune	0.366	0.318	0.684	0.789	0.842
Freeze Encoder	0.330	0.268	0.655	0.763	0.824

Table 3: The dice coefficient of different PEFT methods, trained from default SAM, for medical segmentation and averaged over all 6 datasets. (\*): 1st Place; (\*\*): 2nd Place; (\*\*\*): 3rd Place.

<b>PEFT Method</b>	<b>Point</b>	<b>Box</b>	<b>I<sub>p</sub></b>	<b>I<sub>b</sub></b>
Full FT	*0.723	**0.830	0.811	0.850
Attn Tune	**0.721	*0.810	**0.825	0.855
AdaptFormer	0.612	0.814	0.789	***0.858
LoRA	***0.673	***0.826	*0.838	*0.862
QLoRA	0.386	0.757	0.394	0.508
FacT	0.633	0.812	***0.815	**0.862
SSF	0.592	0.802	0.803	0.850
Bias Tune	0.615	0.810	0.802	0.847
LN Tune	0.596	0.818	0.805	0.843
Freeze Encoder	0.521	0.791	0.784	0.833

Table 4: The dice coefficient of different PEFT methods, trained from MedicoSAM, for medical segmentation and averaged over all 6 datasets. (\*): 1st Place; (\*\*): 2nd Place; (\*\*\*): 3rd Place.

<b>PEFT Method</b>	<b>Point</b>	<b>Box</b>	<b>I<sub>p</sub></b>	<b>I<sub>b</sub></b>
Full FT	*0.709	0.813	0.826	0.868
Attn Tune	***0.687	0.824	**0.862	0.879
AdaptFormer	0.670	0.842	0.856	0.880
LoRA	**0.694	0.836	*0.883	*0.901
QLoRA	0.639	***0.846	***0.856	**0.890
FacT	0.645	**0.849	0.852	0.885
SSF	0.658	0.845	0.853	0.883
Bias Tune	0.643	0.832	0.845	0.881
LN Tune	0.645	*0.850	0.853	0.879
Freeze Encoder	0.583	0.812	0.830	0.879

## B.2. Computational Efficiency

We measure the efficiency of PEFT methods, in terms of number of trainable parameters, training time per iteration and in total, and VRAM memory usage during training. Tab. 5 reports these measures for ViT-B and all PEFT methods, Tab. 6 and Tab. 7 report them for ViT-L and ViT-H respectively, for only a subset of PEFT methods. These results were obtained from finetuning default SAM on the LIVECell (Edlund et al., 2021) dataset, a large dataset with annotations for cell segmentation in phase-contrast microscopy. Note that we perform all experiments for segmentation quality with the smallest model, ViT-B, because it was shown e.g. in (Gu et al., 2024; Archit et al., 2025) that using it does not have a noticeable impact compared to the larger models ViT-L and ViT-H for segmentation quality in biomedical imaging. However, we evaluate the computational efficiency for all model sizes, as this observation may not hold true for other domains, for which finetuning the larger models may be beneficial. We report efficiencies only for a single dataset, as these measurements are largely independent of the data specifics. The exception is the overall training time because we use early stopping. Specifically, we stop the training after 10 epochs without an improvement in the validation score. Hence, the overall training time depends on dataset characteristics. We report the training time across datasets in Fig. 8.

We see that all PEFT methods lead to a clear reduction in the number of trainable parameters, from 30% (Attn Tune) to less than ca. 5% (all others). However, this reduction in trainable parameters does not result in a clear reduction of memory requirements or training time per iteration. This fact is especially noticeable for ViT-B, for the larger models, especially ViT-H, the reduction in memory becomes a bit more pronounced. The exception is freezing the encoder, which clearly reduces the memory demand and also reduces training time per iteration, for all model sizes. It is unclear to us why the reduction in trainable parameters is not accompanied by a similar reduction in memory consumption for other methods.

Table 5: Number of trainable parameters, training times, and allocated VRAM during training for different PEFT methods. Here, Train Time refers to the time until the best epoch is reached during training. Training times and memory are reported for finetuning default SAM with ViT-B on LIVECell. The number of parameters is shown as # Params w/o decoder | # Params with decoder. (\*): selective PEFT; (\*\*): additive PEFT

PEFT Method	#Params [M]	Time / it [s]	Train Time [h]	Memory [GB]
Full FT	93.7   104.8	1.44	14.33	52.1
Attn Tune (*)	32.5   43.5	1.42	19.72	51.4
AdaptFormer (**)	5.3   16.3	1.43	18.75	50.8
LoRA (**)	5.3   16.3	1.44	17.59	51.2
QLoRA (**)	5.3   16.3	1.50	18.34	51.1
FacT (**)	4.4   15.4	1.45	19.60	51.2
SSF (**)	4.3   15.3	1.49	16.12	53.3
Bias Tune (*)	4.2   15.2	1.42	8.34	50.1
LN Tune (*)	4.1   15.1	1.41	15.29	50.9
Freeze Encoder (*)	4.1   15.1	1.24	16.79	35.5

Table 6: Number of trainable parameters, training times, and allocated VRAM during training for different PEFT methods. Here, Train Time refers to the time until the best epoch is reached during training. Training times and memory are reported for finetuning default SAM with ViT-L on LIVECell. The number of parameters is shown as # Params w/o decoder | # Params with decoder.

PEFT Method	#Params [M]	Time / it [s]	Train Time [h]	Memory [GB]
Full FT	312.3   323.4	1.92	21.68	65.8
LoRA	7.2   18.2	1.84	7.49	63.4
QLoRA	7.2   18.2	2.06	7.46	63.3
Freeze Encoder	4.1   15.1	1.37	18.55	36.3

Table 7: Number of trainable parameters, training times, and allocated VRAM during training for different PEFT methods. Here, Train Time refers to the time until the best epoch is reached during training. Training times and memory are reported for finetuning default SAM with ViT-H on LIVECell. The number of parameters is shown as # Params w/o decoder | # Params with decoder.

PEFT Method	#Params [M]	Time / it [s]	Train Time [h]	Memory [GB]
Full FT	641.1   652.1	2.20	27.86	76.9
LoRA	9.3   20.3	2.21	5.98	71.2
QLoRA	9.3   20.3	2.49	7.89	69.7
Freeze Encoder	4.1   15.1	1.51	14.29	37.8

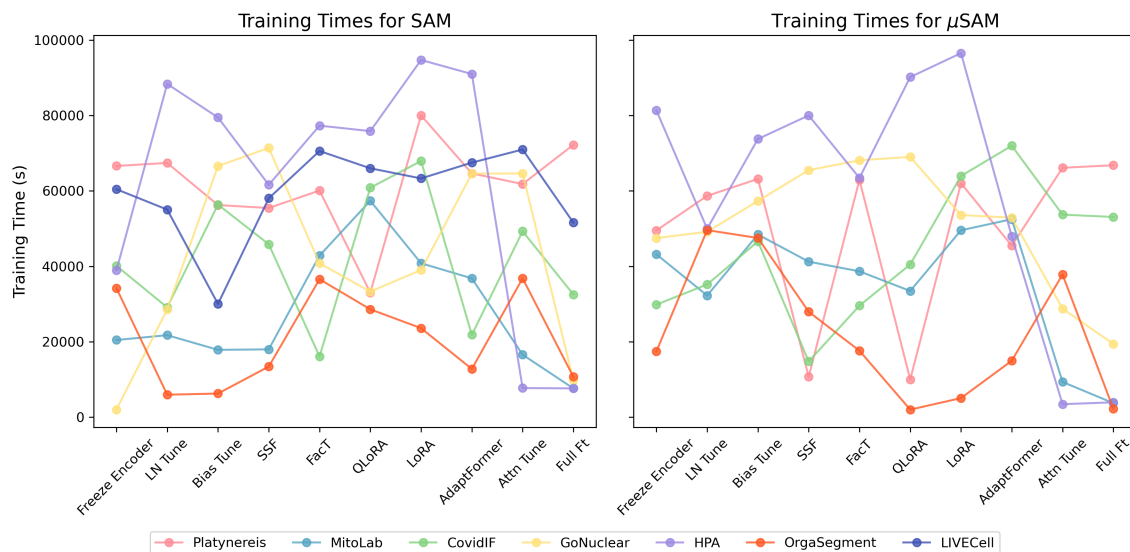


Figure 8: Time until convergence (early stopping) when training  $\mu$ SAM and SAM on the microscopy datasets, including LIVECell, for the PEFT methods.

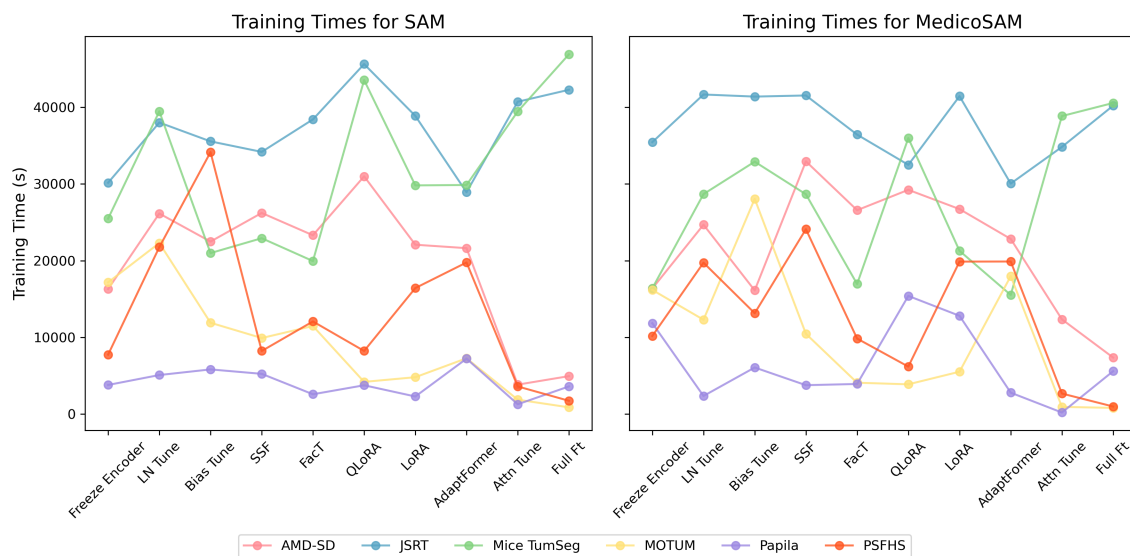


Figure 9: Time until convergence (early stopping) when training MedicoSAM and SAM on the 6 medical datasets for the PEFT methods.



### Appendix C. Resource-efficient Finetuning

Fig. 5 shows the results for training on a single annotated image (with another used for validation). These results show that the performance of LoRA, when trained on a single image is highly dataset-dependent. For datasets like Platynereis (Vergara et al., 2021), which feature sparse instances within a single image, single-image training shows some limitations. Similarly, in the case of 3D datasets such as Platynereis, MitoLab, and GoNuclear, training on a single slice of one volume poses the additional challenge of selecting a suitable slice. However, the performance achieved for MitoLab in this setting was notably strong. Here, when trained from the  $\mu$ SAM model, both LoRA and full fine-tuning achieved a mean segmentation accuracy of 0.54 when trained on a single image. Using all available images outperformed single-image training by only 6% for full finetuning and 2% for LoRA. As shown in Tab. 8, LoRA consistently reduces memory usage by approximately 500 MB compared to full fine-tuning. Thus, in resource constrained training settings, LoRA can be a practical solution, potentially enabling training scenarios that would otherwise be infeasible.

Table 8: Allocated memory (in gigabytes) for each microscopy dataset during training, comparing full fine-tuning, LoRA, QLoRA and freezing the encoder when training from SAM and  $\mu$ SAM.

Allocated Memory [GB]	Covid-IF	Platynereis	MitoLab	OrgaSegment	GoNuclear	HPA
<b>SAM</b>						
Full FT	13.3	13.3	13.3	13.3	13.3	13.3
LoRA	12.8	12.8	12.8	12.8	12.8	12.8
QLoRA	12.5	12.5	12.5	12.5	12.5	12.5
Freeze Encoder	5.8	5.8	5.2	5.8	5.8	5.8
CellSeg1	7.0	7.7	8.4	11.3	9.6	8.0
<b><math>\mu</math>SAM</b>						
Full FT	13.3	13.3	13.3	13.3	13.3	13.3
LoRA	12.8	12.8	12.8	12.8	12.8	12.8
QLoRA	12.6	12.5	12.6	12.5	12.6	12.5
Freeze Encoder	5.8	5.8	5.8	5.8	5.8	5.8
CellSeg1	7.0	7.7	8.3	11.3	9.7	8.0

Table 9: Training time until convergence in minutes for each microscopy dataset, comparing full fine-tuning, LoRA, QLoRA and freezing the encoder when training from SAM and  $\mu$ SAM. For CellSeg1 the training time amounts to approximately 30 minutes, for 300 epochs, without early stopping.

Train Time [min]	Covid-IF	Platynereis	MitoLab	OrgaSegment	GoNuclear	HPA
<b>SAM</b>						
Full FT	3.10	11.32	18.90	16.63	7.50	3.18
LoRA	18.42	10.97	13.65	19.61	10.59	12.55
QLoRA	9.73	10.99	9.79	16.48	12.15	20.69
Freeze Encoder	2.38	19.81	12.77	16.56	10.73	9.38
<b><math>\mu</math>SAM</b>						
Full FT	5.41	8.33	2.35	1.18	5.57	1.04
LoRA	5.34	18.48	3.39	5.55	2.26	3.11
QLoRA	13.20	25.36	2.32	7.04	3.54	2.14
Freeze Encoder	4.67	15.32	0.93	3.67	5.94	6.54

Table 10: Time per iteration in seconds for each microscopy dataset, comparing full fine-tuning, LoRA, QLoRA and freezing the encoder when training from SAM and  $\mu$ SAM.

Train Time per Iteration [s]	Covid-IF	Platynereis	MitoLab	OrgaSegment	GoNuclear	HPA
<b>SAM</b>						
Full FT	0.74	0.71	0.69	0.71	0.69	1.27
LoRA	0.71	0.73	0.68	0.69	0.67	1.25
QLoRA	0.73	0.73	0.73	0.73	0.69	1.31
Freeze Encoder	0.57	0.55	0.55	0.54	0.56	1.13
<b><math>\mu</math>SAM</b>						
Full FT	0.72	0.71	0.71	0.71	0.67	1.25
LoRA	0.71	0.69	0.68	0.67	0.68	1.24
QLoRA	0.75	0.74	0.70	0.70	0.71	1.28
Freeze Encoder	0.56	0.54	0.56	0.55	0.55	1.12

## Appendix D. Ablation Study

## D.1. LoRA

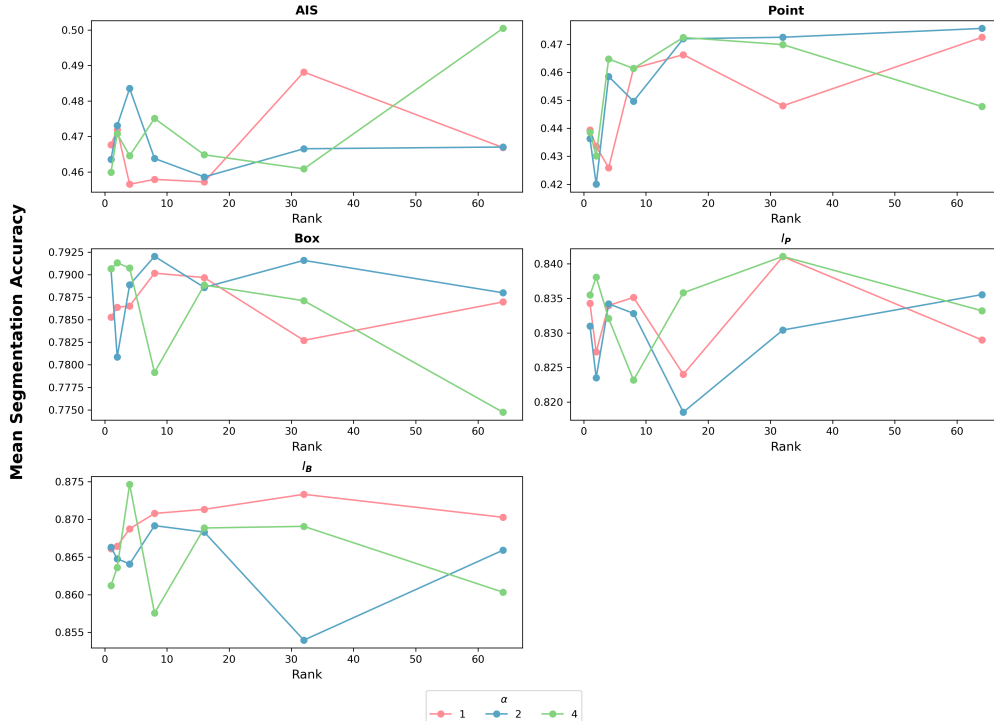


Figure 10: Inference results on OrgaSegment for LoRA with different combinations in  $\alpha$  and rank. Results are shown in mean segmentation accuracy and evaluated across different tasks.

In this section, we conduct a series of experiments to investigate the influence of two key hyperparameters in LoRA: the rank and the scaling factor  $\alpha$ , as described in Section 2.1. Specifically, we aim to understand how these parameters impact segmentation accuracy and model performance.

(Hu et al., 2021) suggest that the scaling factor  $\alpha$  behaves similarly to the learning rate, with both influencing the optimization process and model convergence. We explore this relationship through a series of experiments that vary  $\alpha$  and rank in conjunction with the learning rate.

Figure 10 presents the impact of rank on segmentation accuracy for various values of  $\alpha$ . Intuitively, one might expect that increasing the rank would lead to improved accuracy, as it expands the parameter space. However, our experiments show that rank has only a marginal influence on iterative prompting. However, there is a noticeable improvement in the AIS and single point metrics as rank increases. Based on these findings, we choose a rank of 32 for all other experiments that use LoRA.

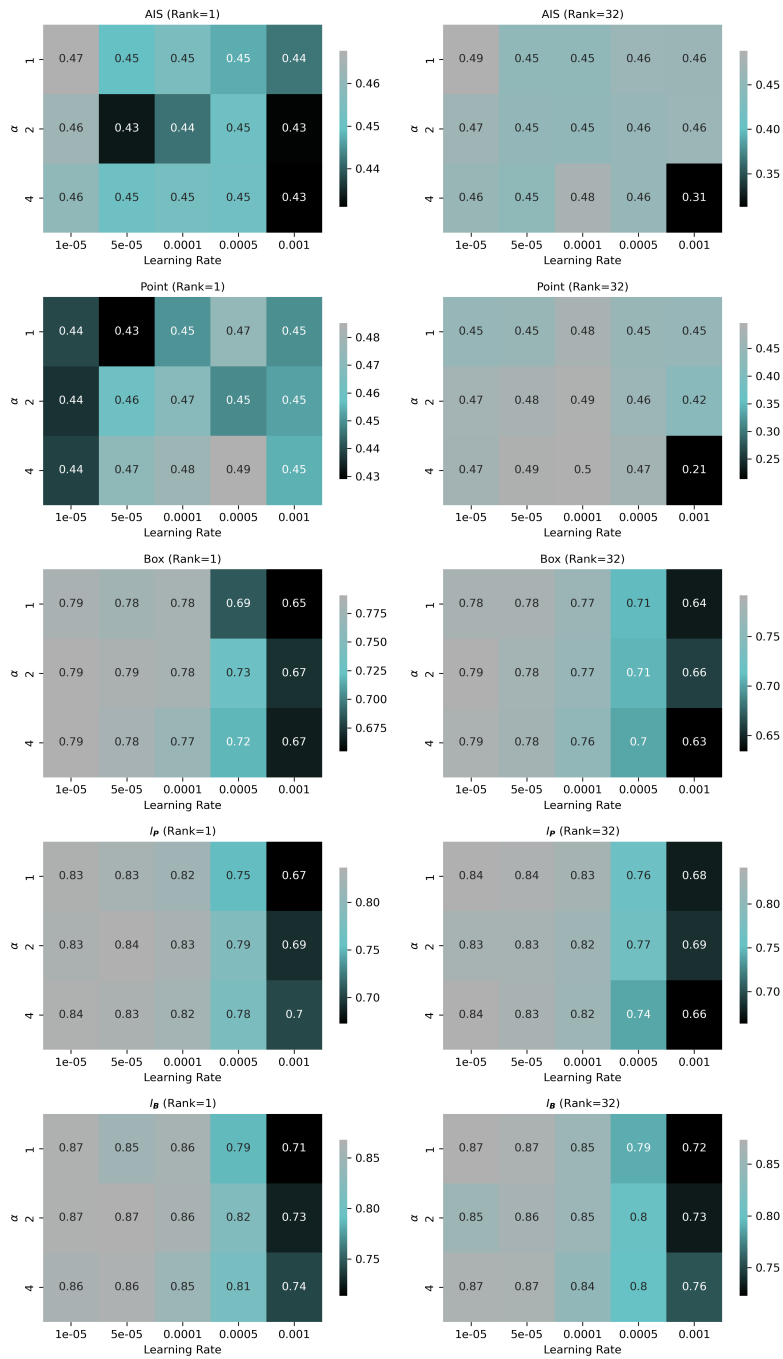


Figure 11: Inference results on OrgaSegment for LoRA with different learning rates and scaling factors  $\alpha$ . The colorbars represent mean segmentation accuracy.

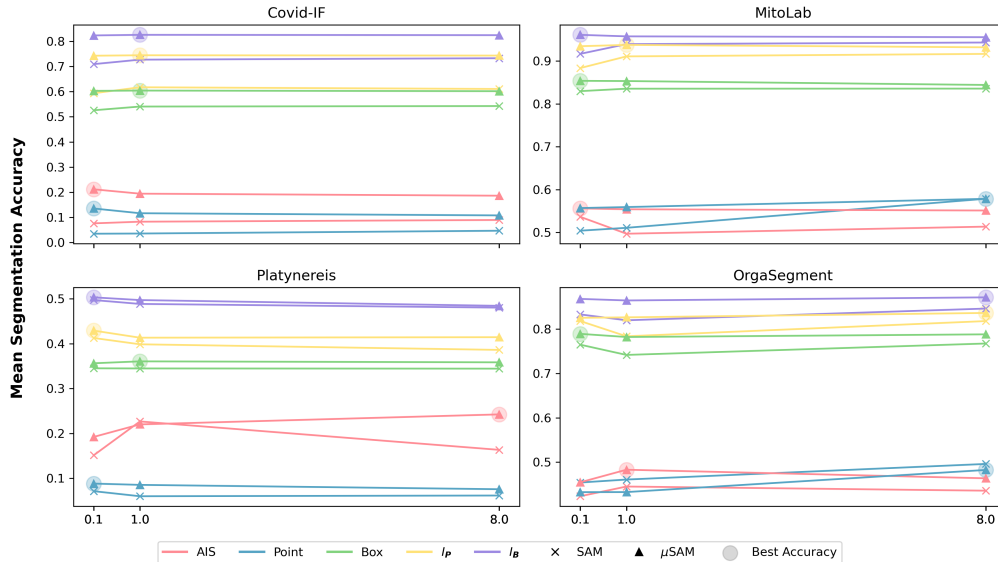


Figure 12: Inference results for LoRA with different scaling factors  $\alpha$  on four datasets. Circles highlight the best results per dataset and task

Next, we investigate the relationship between the scaling factor  $\alpha$  and the learning rate. Figure 11 illustrates that smaller learning rates tend to yield better performance across various values of  $\alpha$ . From this experiment, we select a learning rate of  $1 \times 10^{-5}$  for all further experiments, as it provides the best trade-off between convergence and accuracy.

Our findings also suggest that using both a high learning rate and a large  $\alpha$  simultaneously is detrimental to performance, potentially leading to instability in optimization. However, the precise influence of  $\alpha$  remains ambiguous, as its impact is not as pronounced as that of the learning rate.

To further investigate the role of  $\alpha$ , we run experiments on four different datasets, as shown in Figure 12. The optimal value for  $\alpha$  varies across datasets, and no consistent pattern emerges. However, we observe that using  $\alpha = 1$  does not harm performance in any case, and we recommend using this default value for practical applications. In general, the scaling factor  $\alpha$  appears to have a limited impact on the model’s performance, and tuning it is not always necessary for achieving good results. We conclude:

- Rank has a marginal effect on iterative prompting but improves AIS and weak prompt performance, so we opt for rank 32.
- Learning rate is a more critical factor, with smaller learning rates being more favorable. A high learning rate and high  $\alpha$  should be avoided.
- The optimal  $\alpha$  value is dataset-dependent, but setting  $\alpha = 1$  is a safe and effective choice across all datasets.

## D.2. AdaptFormer

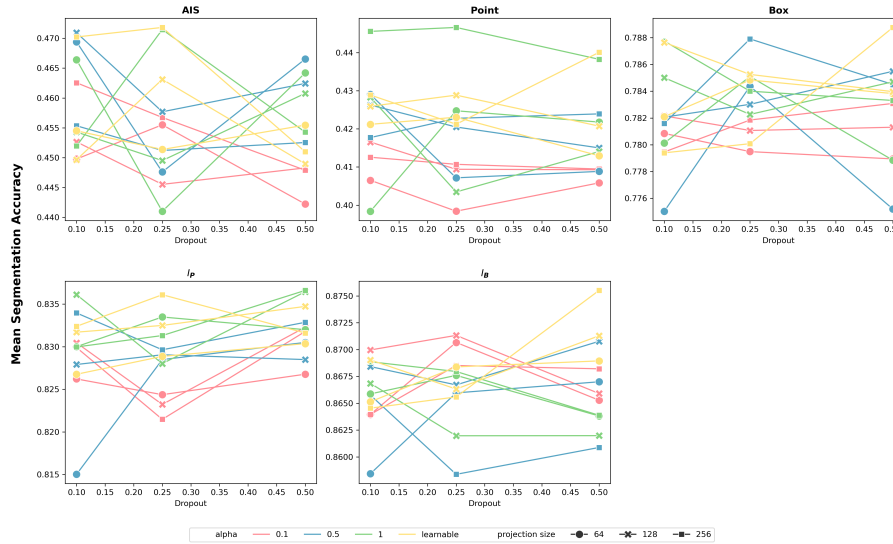


Figure 13: Inference results on OrgaSegment for different projection sizes and scaling factors and dropout values for AdaptFormer.

To find the best hyperparameters for AdaptFormer a grid-search was run on 3 parameters. The scaling factor, which scales the output of the Adapter module and therefore, similarly to LoRA, balances the impact of the features from the frozen branch with the task-specific features from the tunable parameters. Secondly, we try different projection sizes, meaning the middle dimension of the AdaptFormer module, which controls the number of learnable parameters that are introduced by this finetuning method. Lastly we introduce an optional dropout layer, between the down and up projection of the AdaptFormer branch.

Fig. 13 indicates that the dropout factor does not exhibit a consistent pattern in its impact on the inference results. Considering this lack of clarity and the additional stochasticity introduced by dropout during inference, we recommend setting the dropout to None by default, effectively excluding the dropout layer altogether. Assuming that the dropout value does not significantly influence the results, we average across the different dropout settings to achieve a more stable analysis of the alpha values and projection sizes. This is visualized in a heatmap for various inference tasks in figure 14. The results suggest a slight preference for larger projection sizes. However, the performance margin is minimal. Thus, we recommend a smaller projection size of 64 to reduce the number of parameters, balancing performance and complexity.

For the alpha parameter, the best results are observed when it is either learned by the model or set to one. Notably, the alpha values learned by the model are consistently close to one. To maintain flexibility for diverse datasets, we suggest using alpha as a learnable



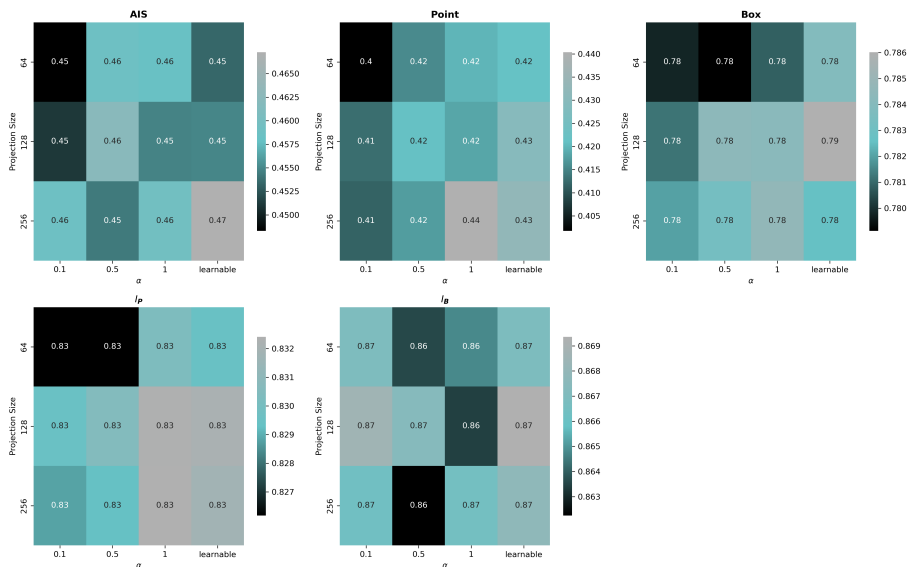


Figure 14: AdaptFormer inference results, trained on OrgaSegment for different scaling factors and projection sizes. The results are averaged over different dropout factor experiments.

parameter. However, if reducing the number of parameters is a priority, setting alpha to 1 is a suitable alternative.

### D.3. FacT

To analyze the impact of hyperparameter tuning in the FacT parameter-efficient fine-tuning method, we conducted an extensive search over two parameters: dropout factor and rank, using the LIVECell dataset. The dropout factor controls an optional dropout layer in the forward function of the FacT methods. We tested dropout factors of 0.1, 0.25, 0.5 and no dropout, finding that a dropout factor of 0.1 achieved the best overall performance. It led to consistent improvements across all tasks. For rank, we observed that increasing its value improved performance up to a rank of 16, which achieved the highest results across most tasks. Further increasing the rank to 32 provided only marginal improvements for weak prompts, while for AIS and iterative prompting, rank 16 remain superior. We therefore recommend using rank 16 for this method.

Table 11: Mean segmentation accuracy for dropout factor and rank parameter search for FacT on LIVECell.

	ais	ip	ib	point	box
<b>Dropout Factor (Rank = 4)</b>					
0.25	0.386388	0.783651	0.828160	0.408460	0.646480
None	0.383379	0.779622	0.822782	0.400679	0.64233
0.1	<b>0.389440</b>	<b>0.787556</b>	<b>0.830561</b>	<b>0.413252</b>	<b>0.649592</b>
0.5	0.385142	0.779190	0.821817	0.397363	0.640852
<b>Rank (dropout=0.1)</b>					
1	0.379699	0.774329	0.822471	0.382696	0.630324
2	0.383812	0.775398	0.822041	0.387330	0.638050
4	0.389440	0.787556	0.830561	0.413252	0.649592
8	0.393855	0.783390	0.826328	0.415375	0.648752
16	<b>0.398600</b>	<b>0.792422</b>	<b>0.833112</b>	0.426964	0.655786
32	0.397353	0.782903	0.831328	<b>0.431270</b>	<b>0.657162</b>